scientific reports

Check for updates

OPEN

Evaluation of deflagration fracturing effect based on the HJC constitutive model

Heng Fan[1], Chenglong Wang[1], Huizhen Liu[2]✉, Weiwei Xiong[1] & Zhonglong Tian[1]

Conventional hydraulic fracturing technology has become a key factor limiting the productivity of offshore oil and gas fields due to its high cost. Therefore, deflagration fracturing technology has emerged as an effective alternative for enhancing production in offshore oil and gas fields, primarily due to its lower costs. The impact load generated by deflagration creates a high-pressure environment, which induces the formation of fractures in the rock. The HJC constitutive model effectively describes the large deformation behavior of rock-like materials under dynamic impact conditions. Therefore, a three-dimensional finite element model of deflagration fracturing was developed using this model to simulate the fracturing process in vertical wells within a low-permeability sandstone reservoir. Under impact loading, a fragmented zone is formed in the rock, and the effective transformation volume of the reservoir is determined by calculating the volume of this fragmented zone. This provides a new evaluation method for assessing fracturing effectiveness, which is then used to evaluate the impact of deflagration fracturing. The results indicate that under impact loading, the deflagration reach ranges from 0.21 to 4.2 m, with a nonlinear relationship between the drug volume and the deflagration reach. As the drug volume increases, both the deflagration reach and the fracturing reforming effect are significantly improved. Furthermore, the drug volume is closely correlated with energy release: larger drug volumes result in greater energy release, larger reforming volumes in the reservoir, and improved fracturing outcomes. Consequently, production capacity is enhanced.

Keywords HJC constitutive model, Deflagration fracturing, Wave propagation, Volume modification

Offshore oil and gas fields can effectively reduce seepage resistance, maximize transformation volume, and increase oil and gas production through fracturing technology, in which hydraulic fracturing plays a crucial role. However, this technology still faces challenges, such as high costs and low efficiency in practical application[1,2]. Conventional hydraulic fracturing can improve the seepage capacity of oil and gas reservoirs to some extent, but the fracture length is typically limited due to the physical properties of the reservoir and water injection development[3,4]. In recent years, deflagration fracturing technology has attracted increasing attention. By utilizing the strong impact generated by the explosions on the surrounding rock, this technology creates an instantaneous high-temperature, high-pressure environment, forming both a fragmented zone and an initial crack zone. This enables efficient reservoir transformation and significantly enhances oil and gas exploitation efficiency[5–7]. Compared to traditional hydraulic fracturing, deflagration fracturing offers higher energy output and creates a more complex crack network, demonstrating great potential for the development of offshore oil and gas fields. Consequently, the fractured zone formed by deflagration fracturing has become a key focus of dynamic rock research[8–10].

In the process of deflagration fracturing, the rock exhibits significant strain rate effects due to the impact force generated by the explosion of explosives[11,12]. The HJC model effectively captures the mechanical behavior of materials under high strain rates and large deformations, requiring fewer parameters and providing clear physical significance, which makes it highly adaptable[13]. The Johnson-Cook model is a widely used empirical model that describes the plastic deformation behavior of materials under high strain rates and high temperature conditions, and it is mainly applied in the field of metallic materials[14–19]. Therefore, the HJC intrinsic model has been widely used in the numerical simulation of deflagration fracturing processes. The evaluation of deflagration fracturing effects involves systematically analyzing crack propagation and assessing the effectiveness of deflagration fracturing technology following its implementation. This evaluation serve as a key indicator of the quality of offshore low-permeability reservoir fracturing operations[20,21]. Moreover, evaluating the effects of deflagration fracturing provides a critical foundation for subsequent oil and gas exploitation and contributes

[1]College of Pipeline Engineering, Xi'an Shiyou University, Xi'an 710065, Shanxi, China. [2]Yongping Refinery of Shaanxi Yanchang Petroleum (Group) Co., Ltd., Yan'an 717208, Shanxi, China. ✉email: lhz2485916980@163.com

to the sustainable development of oil and gas exploration[22]. The evaluation of fracturing effects is an essential component of fracturing engineering. Currently, most studies rely on microseismic monitoring to assess fracturing effectiveness by obtaining relevant parameters related to the modification range of oil wells and fractures through statistics analysis of microseismic events[23–25]. Li Hongmei et al.[26] conducted a comprehensive assessment of the fracturing effect in tight reservoirs within a well zone by analyzing microseismic monitoring events. They applied methods such as fracturing wave analysis and range calculations to evaluate fracture reforming volume, fracture length, width, and other related fracture parameters. Sheng et al.[27] studied the fractal characteristics of reservoir volume fracturing fracturing networks, proposing a stochastic fracture network algorithm that converts microseismic data into fractal geometry. They characterized fracture geometry by setting bifurcation direction and iteration number, and ultimately developed a modified volume method (referred to as ESRV), which is significant for evaluating fracturing effects in shale gas reservoirs. Wang Guoyi et al.[28] priformed microseismic monitoring on 11 layer fracturing wells in the target block, obtaining relevant data such as fracture length, height, and azimuth. After further processing, they completed the evaluation of the fracturing effect. Zhao Chaofen et al.[29] implemented microseismic monitoring on Block J2 of the Liaohe River exploration area, analyzing the length, height and direction of fractured cracks in the target block. Boek et al.[34]. constructed a 1D single-phase Deep Bed Filtration (DBF) model, solved it using the finite volume method, validated it with SEM-EDS and EDD-T experimental data, simulated backflow (including two extreme conditions of complete particle retention/release), and introduced an erosion mechanism to analyze pressure changes. They quantified the impact of drilling fluid particle invasion on reservoir permeability, with calculation results consistent with experiments; reproduced the 30% particle release rate during backflow; confirmed that internal reservoir damage contributes to the Flow Initiation Pressure (FIP), providing theoretical support for formation damage control. The effectively evaluated the fracturing and reservoir reforming effects, providing clear direction for subsequent development. The HJC constitutive model is widely used in the numerical simulation of deflagration fracturing, and microseismic monitoring is commonly employed to evaluate hydraulic fracturing effects. However, the evaluation methods for deflagration fracturing effects remain insufficient. Therefore, this paper proposes a new method for evaluating deflagration fracturing effects based on the HJC constitutive model.

Based on existing theory, a method for evaluating the effects of deflagration fracturing is proposed by considering the impact of explosion shock waves. This method involves a numerical simulation of deflagration fracturing using the HJC constitutive model. LS-DYNA software is employed to establish a finite element model, analyze the influence of the deflagration wave range and the reformed volume on the fracturing process, simulate rock fragmentation, and assess the overall fracturing effect. The goal is to provide a technical guideline for the on-site application of deflagration fracturing technology.

HJC constitutive model

The deflagration fracturing process occurs instantaneously. For the material constitutive model, the rapid change in high strain rate over a short period complicates the selection of an appropriate model. Furthermore, the inherent complexity of rock materials adds another layer of difficulty in choosing a suitable constitutive model. One of the key factors in evaluating the effect of deflagration fracturing is the constitutive model under rock impact loading, making the selection of an appropriate model crucial.

The HJC (Holmquist-Johnson-Cook) constitutive model consists of three components, the equation of state, the strength model, and the damage model, which together involve 21 parameters. These parameters effectively characterize the large deformation behavior of rock materials during dynamic impact processes[30–32].

(1) Strength model.

The strength model of the HJC constitutive model is illustrated in Fig. 1 and is described using normalized equivalent stresses, as expressed by the following equation:

$$\sigma^* = \left[A\left(1-D\right)+B(P^*)^N\right]\left[1+C\ln\left(\frac{\dot{\varepsilon}}{\dot{\varepsilon}_0}\right)\right] \leqslant S_{\max} \tag{1}$$

In the formula, its expression is as follows: The variation range of D is between 0 and 1, and it is a damage variable. When D = 1, it indicates that the rock is completely broken; when D = 0, it indicates that the rock has no damage.

The dimensionless equivalent stress is denoted by σ^*, and its expression is as follows:

$$\sigma^* = \frac{\sigma}{f_c} \tag{2}$$

In the formula, $\sigma$is the actual equivalent stress, and $f_c$is the static uniaxial compressive strength. σ^*can also be expressed by damage.

The dimensionless hydrostatic pressure P^*can be expressed as:

$$P^* = \frac{P}{f_c} \tag{3}$$

In the formula, P represents the actual hydrostatic pressure. The $\dot{\epsilon}^*$dimensionless strain rate can be expressed as:

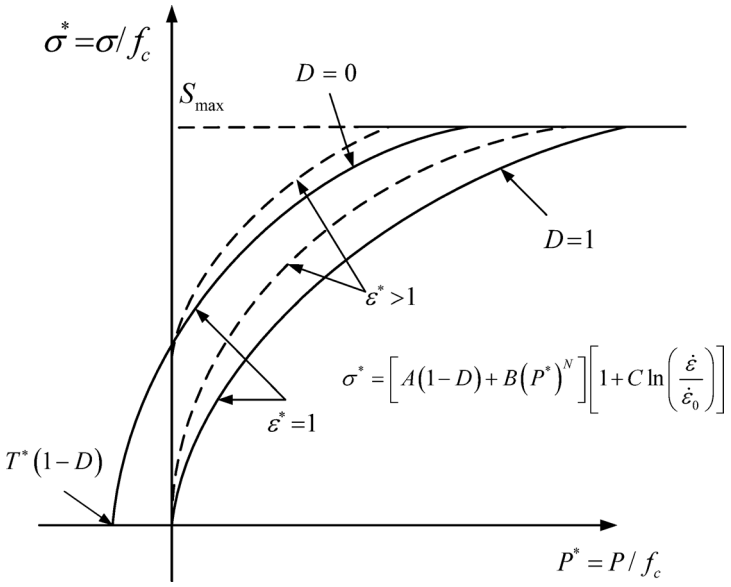

Fig. 1. Strength model.

$$\dot{\varepsilon}^* = \frac{\dot{\varepsilon}}{\dot{\varepsilon}_0} \tag{4}$$

In the formula, ϵ^* denotes the actual strain rate, and $\dot{\epsilon}_0$ denotes the reference strain rate.

The dimensionless maximum tensile stress T^* can be expressed as:

$$T^* = \frac{T}{f_c} \tag{5}$$

In the formula, T represents the maximum tensile stress that the material can withstand.

Where $S_{\max}$is the standardized maximum strength, A is the normalized cohesive strength, B is the normalized pressure hardening coefficient, N is the pressure hardening index, C is the strain rate coefficient, and D is the damage parameter.

(2) Damage model.

In the HJC model, damage results from the accumulation of plastic strain, as described by the damage evolution equation:

$$D = \sum \left(\frac{\Delta\varepsilon_p}{\varepsilon_f}\right) \tag{6}$$

Where $\Delta\varepsilon_p$is the equivalent plastic strain increment of the unit within the cycle, and $\varepsilon_f$is the maximum tensile pressure that the material can withstand.

Generally, the damage factor D and plastic strain ε serve as the basis of unit failure. When the damage factor D or plastic strain ε exceeds a specific threshold, the unit fails, as shown in Fig. 2. The plastic strain threshold is:

$$\varepsilon_p^f + \mu_p^f = D_1(P^* + T^*)^{D_2} \geqslant E_{f\min} \tag{7}$$

Where dimensional tensile strength $T^* = T / f_c$, D_1 and D_2 are material damage parameters, and $E_{f\min}$ is the minimum plastic strain at which material failure occurs.

(3) The equation of state.

The equation of state, as shown in Fig. 3, is divided into three phases: the linear elastic phase, the plastic deformation phase, and the dense phase.

The first stage is the linear elastic phase, which occurs in the early stage of loading, $P < P_c$, exhibiting obvious linear elastic characteristics and satisfying the following relationship:

$$K_e = P_c / \mu_c \tag{8}$$

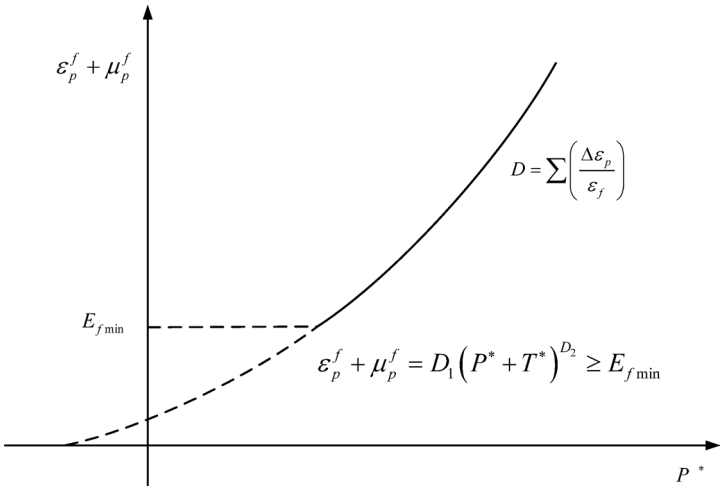

Fig. 2. Damage model.

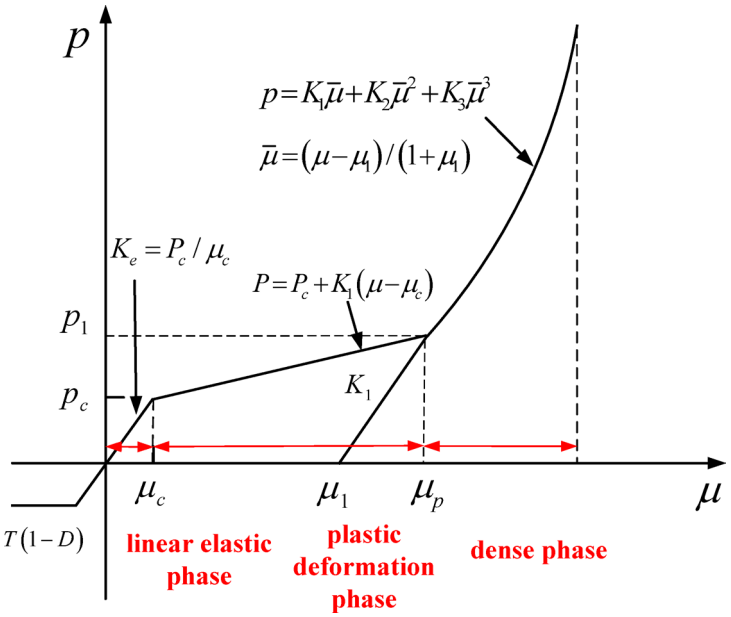

Fig. 3. The equation of state.

Where K_e is the bulk modulus, P_c is the hydrostatic pressure when the material is crushed, and μ_c is the volumetric strain when the material is crushed.

The second stage is the plastic deformation stage, $P_c < P < P_l$, characterized by plastic deformation caused by the compression of micropore defects inside the material, and is describes by the following relationship:

$$P = P_c + K_1(\mu - \mu_c) \tag{9}$$

Where P_c is the hydrostatic pressure at the limit of compaction, and μ_c is the volumetric strain at the limit of compaction.

The third stage is the compaction stage, also as known as the fully fragmented stage, $P > P_l$, which the internal void defects of the material have been filled. This stage fully accounts for the effects of strain rate, damage, and other factors, and the following relationships are satisfied during loading:

$$P = K_1\mu + K_2\mu^2 + K_3\mu^3 \tag{10}$$

Where K_1, K_2 and K_3 are bulk modulus-related coefficients that characterize the elastic volumetric behavior of the material after full compaction, and $\bar{\mu}$ is the modified volumetric strain.

The ALE (Arbitrary Lagrangian-Eulerian) algorithm is adopted. For a non-stationary incompressible fluid, the governing equations of the Navier-Stokes (N-S) fluid can be expressed as follows:

$$\frac{\partial u}{\partial t} + u\nabla u - 2u^F \nabla \varepsilon(u) + \nabla p = b \tag{11}$$

$$\nabla \cdot u = 0 \tag{12}$$

Boundary Conditions:

$$\sigma = -pl + 2\nu^F \varepsilon(u) \tag{13}$$

Initial Conditions:

$$\varepsilon(u) = \frac{1}{2}\left(\nabla u + (\nabla u)^T\right) \tag{14}$$

In the description of the ALE algorithm, an additional arbitrary reference coordinate system is introduced, and the material derivative associated with this coordinate system is defined as:

$$\frac{\partial f(X_i, t)}{\partial t} = \frac{\partial f(x_i, t)}{\partial t} + w_i \frac{\partial f(x_i, t)}{\partial x_i} \tag{15}$$

Herein,X_i denotes the Lagrangian coordinate, x_i represents the Eulerian coordinate, andw_i stands for the relative velocity.

Let ν be the material velocity, u be the grid velocity, and w be the relative velocity, where$w = \nu - u$. Then, the governing equations of the ALE algorithm can be expressed as:

(1) Mass conservation equation:

$$\frac{\partial \rho}{\partial t} = -\rho \frac{\partial \nu_i}{\partial x_i} - w_i \frac{\partial \rho}{\partial x_i} \tag{16}$$

(2) Momentum conservation equation:

In the enhanced form of Newtonian fluids, there are three core elements: governing equations, boundary conditions, and initial conditions. Within the framework of the ALE algorithm, the Navier-Stokes (N-S) equations can be re-expressed as:

$$\nu \frac{\partial \nu_i}{\partial t} = \sigma_{ij,j} + \rho b - \rho w_i \frac{\partial \nu_i}{\partial x_j} \tag{17}$$

Stress tensorσ_{ij}:

$$\sigma_{ij} = -p\delta_{ij} + \mu\left(\nu_{i,j} + \nu_{j,i}\right) \tag{18}$$

Boundary conditions:

$$v_i = U_i^0, in\ the \mathbf{\Gamma}_1\ time\ domain \tag{19}$$

$$\sigma_{ij} n_j = 0, in\ the \mathbf{\Gamma}_2\ time\ domain \tag{20}$$

Wherein, $\Gamma_1 \cup \Gamma_2 = \Gamma, \Gamma_1 \cap \Gamma_2 = 0$. Γ is the complete boundary, while Γ_1 and Γ_2 are partial boundaries of Γ. The superscript 0 denotes the initial configuration. An outward normal vector is defined on the boundary, with the unit vector denoted as n_j, $\delta_{ij}$is the Kronecker delta function. It is assumed that the velocity field is known at time t = 0, which serves as the initial condition:

$$\nu_i(x_i, 0) = 0 \tag{21}$$

(3) Energy conservation equation:

$$\rho \frac{\partial E}{\partial t} = \sigma_{ij}\nu_{i,j} + \rho b_i \nu_i - \rho w_j \frac{\partial E}{\partial x_j} \tag{22}$$

There are mainly two methods for solving ALE equations. The first is to directly solve the fully coupled equations based on fluid mechanics principles; the second adopts operator splitting technology, dividing the calculation at each time step into two stages. First, a Lagrangian process is executed where the mesh dynamically adjusts with material motion to ensure that materials do not cross element boundaries, thereby guaranteeing mass conservation. During this process, the equilibrium equations for calculating the changes in velocity and internal energy are as follows:

$$\rho \frac{\partial \nu_i}{\partial t} = \sigma_{ij,j} + \rho b_i \tag{23}$$

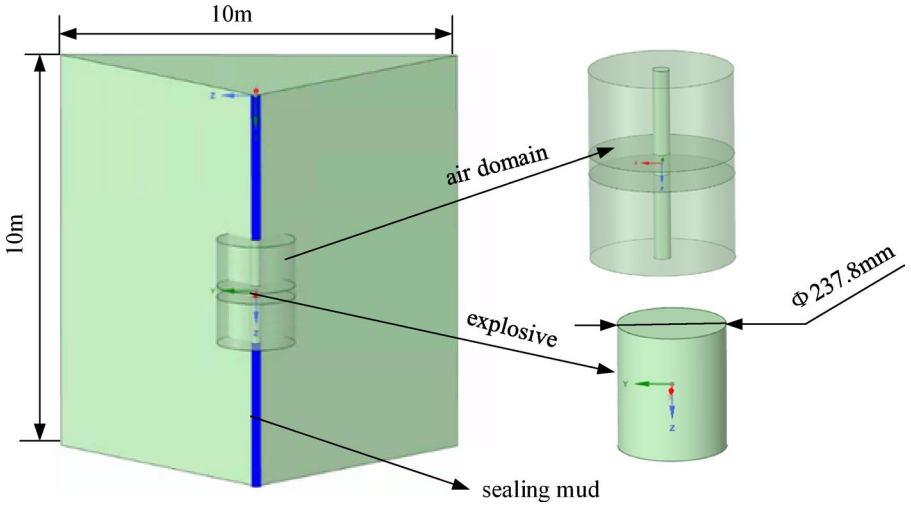

Fig. 4. Finite element model.

ρ_c/(kg·m^{-3})	A/GPa	PCJ/GPa	B/GPa	R_1	R_2	ω	E_0/GPa
1640	113.2	21	1	4.15	0.95	0.3	7

Table 1. Explosive material parameters[33].

$$\rho \frac{\partial E}{\partial t} = \sigma_{ij}\nu_{i,j} + \rho b_i \nu_i \tag{24}$$

Next, for the fluid phase, the mass, internal energy, and momentum of the material passing through element boundaries are calculated.

In the ANSYS/LS-DYNA software, the ALE algorithm is applicable to two element types: PLANE162 and SOLID164. Generally, compared with the PLANE162 element corresponding to 2D ALE equations, the SOLID164 element corresponding to 3D ALE equations exhibits higher stability and reliability. For this reason, when analyzing 2D problems, it is generally preferable to use the 3D SOLID164 element and apply node constraints in the depth direction, thus avoiding the use of the 2D PLANE162 element.

Deflagration fracturing model

Model Building

Based on the physical property tests, mechanical experiments, uniaxial compressive strength tests, and triaxial rock mechanics tests conducted on the core samples from the target block, the rock physical parameters including porosity, permeability, elastic modulus, and the maximum pressure the rock can withstand were obtained. Meanwhile, core samples matching the target Block 8 were selected. Subsequently, an axisymmetric finite element model for deflagration fracturing was established using LS-DYNA R13.0software(https://lsdyna.ansys.com/), as shown in Fig. 4. Since the actual reservoir transformation area is more complex, it is simplified to a square shape for easy of analysis. The dimensions of the formation are 10 × 10 × 10 m, the inner diameter of the wellbore is 237.8 mm, the radius of the air domain is 0.5 m, and its height is 1.32 m. The diameter of the explosive is 237.8 mm, and the explosive mass is 45 kg, with a central detonation method adopted. The rock, air, and explosives are discretized into high-quality hexahedral meshes using the sweep method in WORKBENCH. To better observe the damage area, the explosives are arranged in a region with finer grid cells to improve calculation accuracy. The unit system used in the numerical model includes length in meters (m), time in seconds (s), mass in kilograms (kg), and pressure in Pascals (Pa).

For large deformation problems, such as blast shock waves and rock fragmentation, the multi-material adaptive Lagrange-Euler (ALE) algorithm can not only effectively avoids mesh distortion but also better tracks the interfaces of multiple materials, compared to the traditional Lagrange and Eulerian algorithms. Therefore, the ALE algorithm for the simulation in this study.

The material models for the ALE part include both the explosive and the air. The explosive is described using the * MAT-HIGH-EXPLOSIVE-BURN material model and the * EOS-JWL equation of state, while air is characterized by the * MAT-NULL material model and the * EOS-LINEAR-POLYNOMIAL equation of state for ideal gases. The relevant material parameters are provided in Tables 1 and 2.

ρ_c/(kg·m^{-3})	C_0	C_1	C_2	C_3	C_4	C_5	C_6	E_0/GPa
1.29	0	0	0	0	0.4	0.4	0	0.025

Table 2. Air material parameters[33].

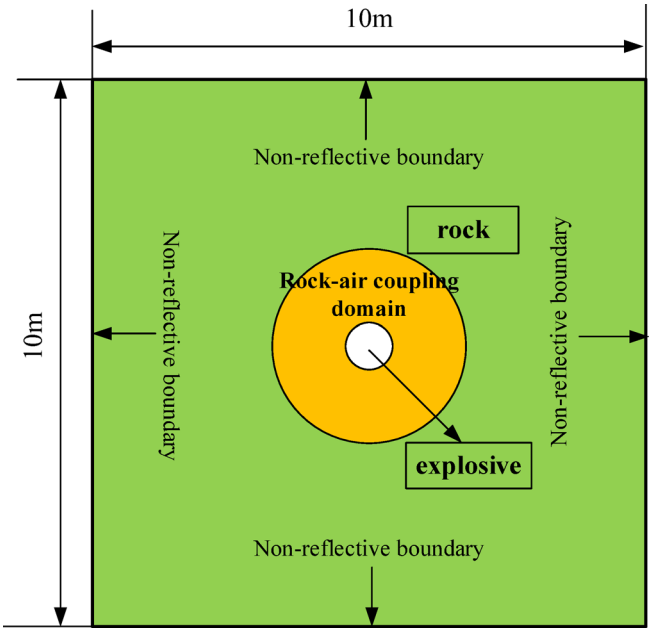

Fig. 5. Boundary conditions.

Hypothetical conditions

In the study of the deflagration fracturing model, the following basic assumptions are made to simplify the complex physical process and facilitate the analysis and calculation of the model:

(1) The deflagration space in the wellbore is confined, and the volume remains constant over time.
(2) The deflagration loading is an adiabatic, isentropic process.
(3) The deflagration is complete, and the components of the deflagration products remain unchanged.
(4) The deflagration follows the law of geometric combustion.

Boundary conditions

Rock blasting typically occurs in an infinite or semi-infinite space. Due to the finite nature of the computational domain, stress waves are reflected at the boundaries, which can affect the stress and strain distribution. Therefore, non-reflecting boundaries are implemented to simulate the effect of an infinite domain, thereby avoiding interference from stress wave reflections and improving simulation accuracy. In this study, all sides of the stratum are treated as non-reflecting boundary conditions, with the bottom surface of the stratum model constrained and the upper surface free. The nonlinear coupling between the explosive shock wave and the rock is modeled using the *CONSTRAINED_LAGRANGE_IN_SOLID keyword, and the boundary conditions are shown in Fig. 5.

Evaluation of the effectiveness of deflagration fracturing

In this study, simulation of deflagration fracturing under impact loads with different charges (10 kg, 20 kg, 30 kg and 45 kg) were carried out in vertical wells. The effect of charge size on the range of deflagration fracturing and the volume of reservoir reforming was analyzed to evaluate the fracturing effect.

Impact of wave propagation on fracturing effectiveness

The range of the deflagration wave under different charges was studied for the four target blocks, and their geomechanical parameters are shown in Table 3.

The deformation of the rock during fracturing is characterized by plastic damage, which involves large, gradual deformation. This process is slow, permanent, and unrecoverable. In sandstone reservoirs, explosive fracturing utilizes the rapid combustion of gunpowder in the wellbore to generate a large volume of high-temperature, high-pressure gas. This pulse loading method involves a significant energy release, making it more suitable for reservoir fracturing and reforming. For target block 2, the damage zone in the reservoir caused by impact loading with a 45 kg charge is shown in Fig. 6.

Target block	Young modulus(GPa)	Densit(g·cm^3)	Poisson's ratio	Porosity(%)
Block 1	9.4 ~ 12.3	2.36 ~ 2.40	0.13 ~ 0.15	14.2–17
Block 2	11.8 ~ 16.6	2.45 ~ 2.53	0.17 ~ 0.26	7.0 ~ 11.4
Block 3	10.5 ~ 16.9	2.375	0.10 ~ 0.14	13.9 ~ 24.5
Block 4	17.2 ~ 20.6	2.47 ~ 2.51	0.19 ~ 0.26	8.0 ~ 15.9

Table 3. Geomechanical parameters of the target blocks.

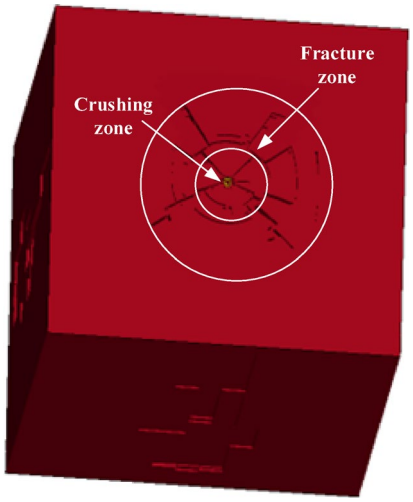

Fig. 6. Reservoir damage zone at 45 kg explosive charges.

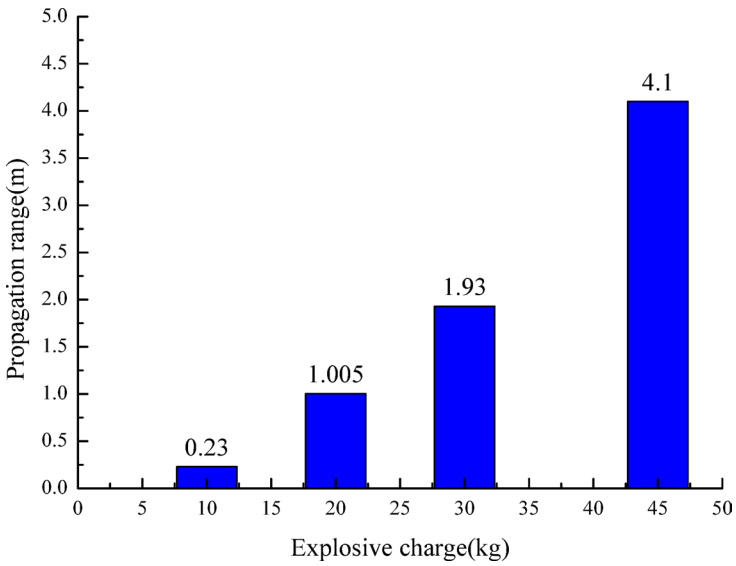

Fig. 7. Propagation range of deflagration fracturing at different explosive charges.

Under impact loading, stress concentration occurs near the wellbore. When the stress in this region exceeds the compressive strength of the rock, it leads to crushing damage. Outside the crushing zone, the circumferential tensile stress generated by the stress wave surpasses the tensile strength of the rock. Due to the high loading rate, this contributes to the formation of multiple fissures. The range of deflagration fracturing waves under different loading rates in target block 2 is shown in Fig. 7.

As shown in Fig. 7, the difference in the range of deflagration fracturing under four charge size is significant, indicating that charge size has a strong influence on the range of deflagration fracturing in vertical wells. This is because the range of deflagration fracturing is directly related to the energy released during the combustion of the explosives, with different charge size corresponding to different amounts of energy releases. Variations

in energy release affect both the strength and range of the deflagration fracturing, ultimately determining the propagation and extension of fractures in the formation. In vertical wells, as the charge size increases, the range of deflagration expands, leading to a better fracture reforming effect. The relationship between charge size and deflagration range is nonlinear, with a significant increase in range when the charge reaches 30 kg. This is due to the fact that a larger charge releases more energy, generating a stronger shockwave and high-pressure gas, which results in longer fractures in the formation. When the charge is 10 kg, the deflagration range is only 0.23 m. However, when the charge is increased to 45 kg, the range can reach 4.1 m, resulting in significant damage rock damage.

To investigate the relationship between the charge size and the deflagration wave range in different blocks, the corresponding graph is presented in Fig. 8.

As shown in the figure, under deflagration impact loading, the deflagration reach increases with the charge size for the same block. However, due to significant differences in geological conditions and reservoir properties between blocks, the deflagration reach varies across different blocks. Therefore, when performing deflagration fracturing to enhance production capacity in offshore oil and gas fields, it is crucial consider the geological characteristics of each block in order to optimize the charge volume and achieve the best deflagration effect.

Impact of volume modification on fracturing effectiveness

The volume of reservoir reforming is influenced by the extent crack propagation. In the early stage of deflagration, the pressure wave area is small, and the impact is primarily concentrated near the wellbore. However, as the deflagration process progresses, the cracks extend and expand, causing the affected area to gradually increase. At the end of the deflagration process, the reservoir transformation volume is shown in Fig. 9. The size of this volume directly reflects the final effectiveness of deflagration fracturing.

Explosive fracturing technology generates high-temperature and high-pressure gas within the reservoir, leading to rock fragmentation and crack formation. This process not only alters the original volume of the reservoir but also increases its pore space due to crack expansion of cracks. However, the overall volume decreases because of the fragmentation of the rock. A detailed analysis of the explosive fracturing process in target block 2 is provided, and the trend in reservoir volume change over time is shown in Fig. 10.

The broken volume is a crucial parameter for assessing the extent of reservoir destruction, as it provides a direct indication of the effectiveness of deflagration fracturing. For example, in the case of a 45 kg charge in target block 2, the initial reservoir volume is 1000m^3, which decreases to 878.42m^3 after deflagration, indicating a rock fragmentation of 121.58m^3. This suggests a relatively favorable outcome for reservoir fracturing. The reduction in reservoir volume during deflagration fracturing is primarily attributed to rock fragmentation and the formation of fractures. Explosive fracturing generates high-energy gas that produces high-temperature, high-pressure shock waves, leading to rock fragmentation around the wellbore and the development of multiple radial cracks. As the process progresses, debris and particles resulting from rock fragmentation fill the fractures, causing a localized reduction in the reservoir volume. Moreover, the high-pressure environment induced by deflagration alters the rock's pore structure, resulting in a decrease porosity, which further contributes to the reduction in reservoir volume.

To clarify the changes in reservoir volume, the volume-time curves for four different loading volume were plotted, as shown in Fig. 11.

As shown in the figure, there is a direct relationship between charge volume and energy release: smaller charge volumes result in less energy release and a smaller transformation of the reservoir volume. When the time is within 0.001s, changes in loading volume have almost no effect on the reservoir volume. However, between

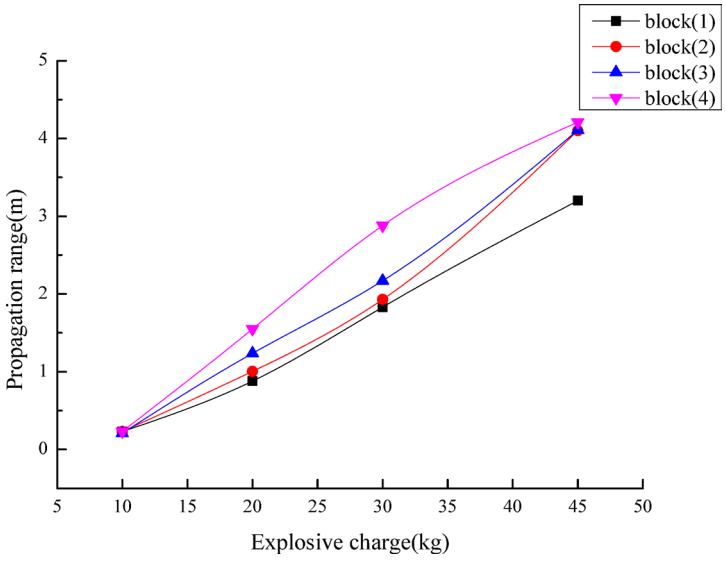

Fig. 8. Relationship between target block propagation range and explosive charge.

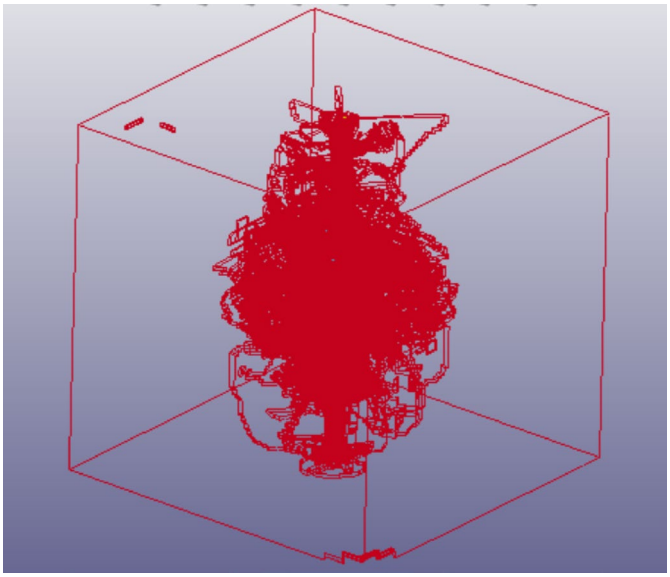

Fig. 9. Reservoir transformation volume at 45 kg explosive charge.

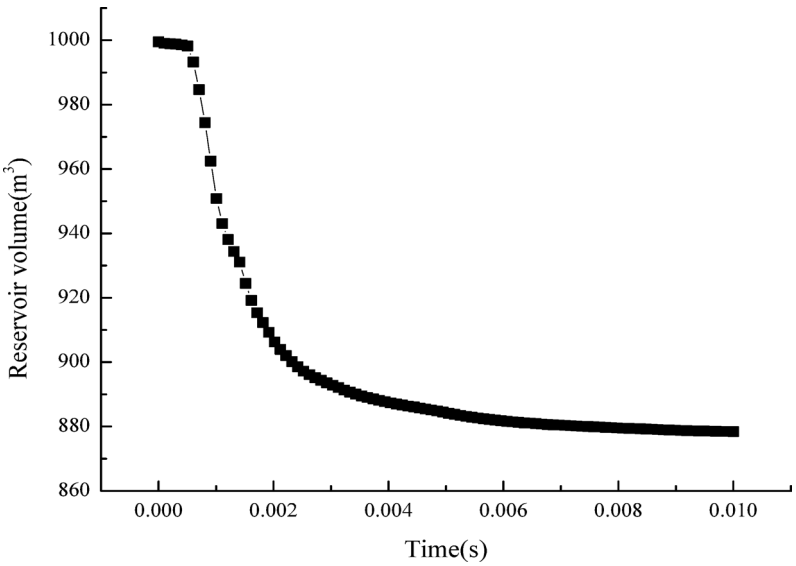

Fig. 10. Target Block 2 reservoir volume changes over time.

0.001 and 0.004s, cracks continue to expand, leading to a significant reduction in the reservoir volume. The effect is more pronounced with larger loading volumes. After 0.004s, crack expansion ceases, and the change in reservoir volume stabilizes.

The specific values of reservoir transformation volume for different explosive doses in the target block are shown in Table 4, with the corresponding trend illustrated in Fig. 12.

As shown in the figure above, the reservoir transformation volume increases with the loading volume. When the charge volume is 10 kg, the transformation effect in the target block is minimal, with the transformation volume ranging from 0.99 to 1.04 m^3. When the charge increases to 30 kg, the transformation volume ranges from 46.36 to 94.9 m^3. At a charge volume of 45 kg, the transformation volume increases significantly, ranging from 86.71 to 153.94 m^3. Therefore, selecting the appropriate charge volume is crucial for evaluating the effectiveness of deflagration fracturing in enhancing the production capacity of offshore oil and gas fields.

Conclusion

In the exploration of production enhancement technologies for offshore oil and gas fields, deflagration fracturing technology has gained attention due to its cost effectiveness. This study aims to simulate the deflagration

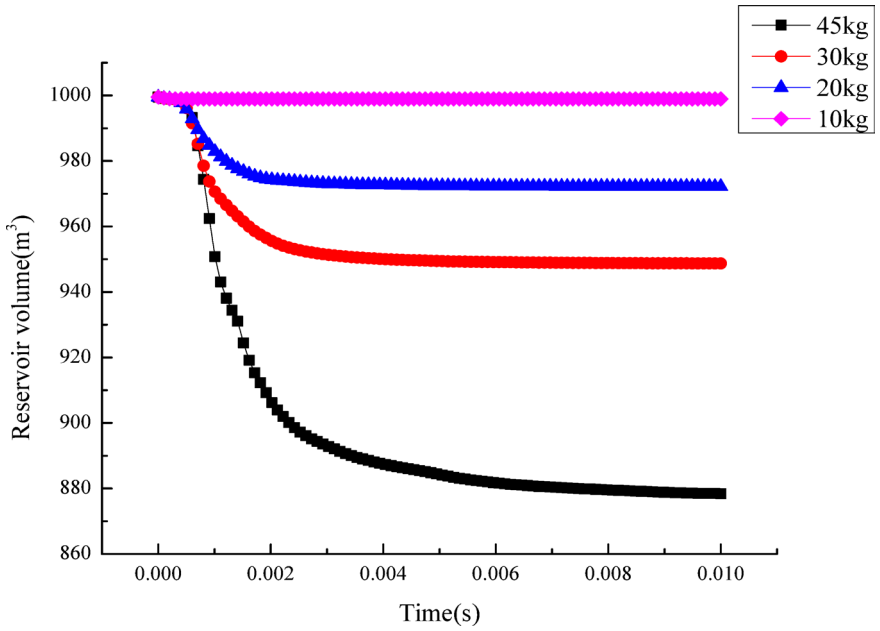

Fig. 11. Reservoir volume curve over time for different explosive charges in target block2.

Target block	Transformed volume(m^3)			
	10 kg	20 kg	30 kg	45 kg
Block 1	0.99	27.93	46.36	86.71
Block 2	1.02	27.76	51.28	121.58
Block 3	1.03	30.32	57.6	140.24
Block 4	1.04	38.44	94.9	153.94

Table 4. Reservoir transformed volume under different explosive charges in the target blocks.

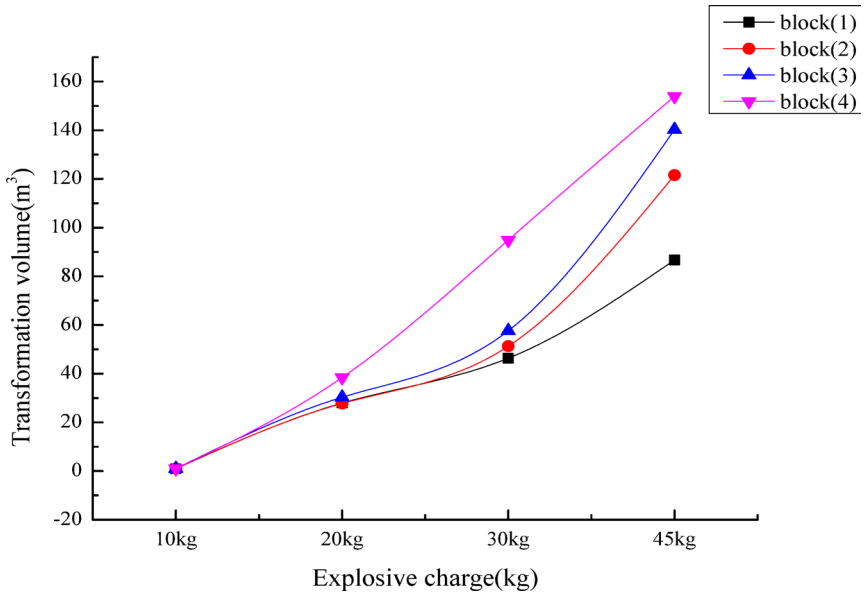

Fig. 12. Curves of transformed volume changes with explosive charges.

fracturing in vertical wells within low-permeability sandstone reservoirs by establishing a three-dimensional finite element model based on the HJC intrinsic model, with the goal of analyzing its fracturing effect.

(1) The HJC damage model accurately describes rock fragmentation behavior under high strain rates. When the damage factor D or plastic strainε exceeds a specific threshold, the model predicts the failure and fragmentation of the rock unit, thereby enabling the calculation of rock fragmentation volume.

(2) The simulation results indicate that the range of deflagration wave propagation is between 0.21 and 4.2 m. Under the influence of the deflagration impact load, a non-linear relationship exists between explosive dosage and wave propagation. For the same block, as the explosive dosage increases, the range of deflagration wave propagation enlarges, thereby enhancing the fracturing and reforming effects. Moreover, due to variations in geological conditions and reservoir characteristics across blocks, the impact of deflagration wave propagation on the blocks differs.

(3) During the deflagration fracturing process, the reduction in reservoir volume is primarily due to rock fragmentation and fracture formation. In target block 2, the initial reservoir volume was 1000m^3 at a 45 kg charge, which decreased to 878.42m^3 by the end of deflagration, indicating a fragmentation volume of 121.58m^3. This suggests a significant fracturing effect. The charge volume is directly related to energy release: as the charge volume increases, more energy is released, leading to a greater reservoir reforming volume and more effective fracturing. Therefore, explosive fracturing serves as an effective means of enhancing oil and gas production.

The influence of explosive charge size essentially lies in the matching relationship between energy input and the formation's bearing threshold. When a certain characteristic of the formation becomes a key bottleneck in energy transfer or consumption, the explosive charge size becomes the dominant factor. For tight low-permeability formations (Block 2), the explosive charge size dominates the initiation and propagation of fractures. For such formations, the minimum explosive charge size must be determined primarily based on the fracture pressure threshold obtained from core tests to avoid fracturing failure due to insufficient energy. The influence of deflagration wave propagation essentially stems from the adaptability between the energy transfer path and the formation structure. Differences in lithological interfaces and stress distributions in specific sequences can alter the propagation speed and attenuation law of deflagration waves, making them the dominant factor.

Outlook

The main research object of this paper is offshore oil and gas fields with tight sandstone as the reservoir geological condition, while the research on other types of reservoirs and microscale fields is still immature. Our team will focus on the general applicability of this model to different reservoirs and research in the microscale field in the subsequent work. Furthermore, I believe that if the HJC simulation can be combined with artificial intelligence models, it will not only improve production efficiency but also contribute to safe production, and this direction still requires the joint efforts of all researchers.

Data availability

The datasets generated and analyzed in this study are not publicly available due to the signed confidentiality agreement, but are available from the corresponding author upon reasonable request.

Received: 13 September 2025; Accepted: 18 November 2025
Published online: 06 January 2026

References

1. Zhang, M. et al. Evaluation technology of hydraulic fracturing effect for offshore oil and gas fields with array acoustic logging [J]. *J. Yangtze University(Natural Sci. Edition)*. **20** (06), 21–29 (2023).
2. Wang, M. et al. Accurate evaluation method of hydraulic fracture height in offshore tight sandstone reservoir [J]. *China Offshore Oil Gas*. **28** (6), 34–39 (2016).
3. Qin, R., Yu, J. & Huang, T. A post-fracturing productivity appraisal technology for tight sandstone gas reservoirs using logging data: taking Linxing block of Ordos basin as an example [J]. *China Offshore Oil Gas*. **31** (1), 67–76 (2019).
4. Bian, X. et al. Evaluation of hydraulic fracturing technology in offshore low permeability reserviors [J]. *Sci. Technol. Eng.* **11** (34), 461–464 (2011).
5. Ming, X. et al. Numerical simulation research on downhole high energy gas fracturing design [J]. *J. Ordnance Equip. Eng.* **42** (05), 158–162 (2021).
6. Chen, H. et al. Research- application of perforating high energy gas fracturing technology [J]. *Drill. Prod. Technol.* **43** (3), 67–69 (2020). 5.
7. Jiwei, W. et al. Numerical study of the fracture propagation mechanism of staged methane deflagration fracturing for horizontal wells in shale gas reservoirs [J]. *Geoenergy Sci. Eng.* **230**, 212209 (2023).
8. Liu Jinghua, H. & Guoqing, J. Production analysis and optimal design of explosive fracturing technology for low permeability reservoir [J]. *Explosion Shock Waves*. **36** (02), 224–229 (2016).
9. Fan, Y. et al. Collision mechanism and rock-breaking effect of explosive stress wave under staggered detonation [J]. *Explosion Impacts*. **44** (06), 92–104 (2024).
10. Wu Feipeng, L. et al. Formation mechanism and main controlling factors of rock's initial damaged zone under explosive impact effect [J]. *Explosion Impacts*. **36** (05), 663–669 (2016).
11. Li, X. et al. Influence of blasting load directions on tunnel stability in fractured rock mass [J]. *J. Rock Mech. Geotech. Eng.* **14** (02), 346–365 (2022).
12. Liu Kai, W. et al. A modified HJC model for improved dynamic response of brittle materials under blasting loads. *Comput. Geotech.* **123**, 103584 (2020)
13. Du, C., Song, S. & Zhang, J. Comparative study on three concrete constitutive models under blast loading [J]. *J. Weapons Equip. Eng.* **43** (11), 49–56 (2022).
14. Sun, L. et al. Optimization and application of multi-stage optimal and fast deflagration fracturing technology in the medium and deep wells of offshore oilfield [J]. *China Offshore Oil Gas*. **36** (01), 125–133 (2024).
15. Hong, B. et al. Development and experimental validation of the dynamic constitutive model and equation of state for Mo-10Cu alloy [J]. *Defence Technology*. **51**(09):145–158. (2025).

16. Li, Y. et al. Thermal deformation behavior of cu-sn alloys based on the modified johnson-cook constitutive model[J/OL]. *Nonferrous Metals Science and Engineering*, 1–10. https://link.cnki.net/urlid/36.1311.tf.20250819.1527.004 (2025).
17. Wang, X. B. et al. Study on mechanical properties of DT600 ultra-high strength steel and fitting of Johnson-cook constitutive parameters [J]. *J. Ordnance Equipment Engineering*. **46**(08): 80–88. CNKI:SUN:CUXI.0.2025-08-010. (2025).
18. Shao, H. T. et al. Johnson-cook constitutive model and comparative analysis of 22MnB5 high-strength steel with Al-Si coating [J]. *Hot Working Technol.* **54** (16), 187–191. https://doi.org/10.14158/j.cnki.1001-3814.20212187 (2025).
19. Li, W. H. et al. Dynamic current-carrying mechanical properties of Cu-Cr-Zr alloy and its modified johnson-cook model[J/OL]. *J. Xi'an Jiaotong Uni.* 1–8. https://link.cnki.net/urlid/61.1069.T.20250625.1118.002 (2025).
20. Sun, L. et al. Application of deflagration fracturing technology in plug removal by screen pipe well completion [J]. *China Offshore Oil Gas*. **33** (04), 143–148 (2021).
21. Sun, L. et al. Research and field test of deflagration fracturing technology in offshore oilfields [J]. *Petroleum Drill. Techniques*. **47** (05), 91–96 (2019).
22. Li, D., Li, C. & Yuan, Q. Evaluation of fracturing effect of horizontal wells in coal shale gas based on borehole micro-seismic rapid location monitoring technology——take well J1HF in South North China as an example [J]. *Progress Geophys.* **39** (01), 207–215 (2024).
23. Feng Ankang. *Research on Evaluation Method of Fracturing Effect in Tight Reservoirs Based on Deep Learning [D]* (Yangtze University, 2023).
24. Lei Yang. *Research on the Evaluation Method of the Reconstruction Effect of Horizontal Well Volumetric Fracturing [D]* (North east Petroleum University, 2019).
25. Zhu et al. *Intelligent Identification Method and Application of Fractured Cracks in ultra-low Permeability Reservoir Based on Microseismic Monitoring [D]* (China University of Petroleum, 2023).
26. LI Hongmei. Application of micro-seismic monitoring technology to unconventional hydrocarbon reservoir fracturing evaluation [J]. *Petroleum Geol. Recovery Effi.* **22** (3), 129–134 (2015).
27. Sheng, G. et al. Application of fractal geometry in evaluation of effectives stimulated reservoir volume in shale gas reservoirs [J]. *Fractals* **25** (1), 1740007 (2017).
28. Wang Guoyi, W. E. I. et al. Evaluation of hydraulic fracturing effect of CBM well in Gujiao area of Taiyuan Xishan coalfield [J]. *Coal Sci. Technol.* **46** (6), 155–159 (2018).
29. Zhao, C. et al. Adjustment and effectiveness of oilfield development programme based on microseismic monitoring technology–taking Liaohe prospect J2 block as an example [J]. *Progress Geophys.* **37** (01), 320–327 (2022).
30. Long Yu. *Experimental and Numerical Simulation Study on Impact Characteristics of Sandstone Under Acidic Solution Abstract [D]* (North University of China, 2023).
31. Tian, X. et al. Modification and application of limestone HJC constitutive model under the impact load [J]. (Lithosphere, 2021) (Special 7): 6443087. (2022).
32. Liu, K. et al. A modified HJC model for improved dynamic response of brittle materials under blasting loads [J]. *Comput. Geotech.* **123**, 103584 (2020).
33. Wang, P. et al. Numerical simulation study on dynamic response of backfill based on KCC model-ALE algorithm [J]. *Industrial Minerals&Processing*. **54** (01), 39–48 (2025). 2025.01.006.
34. Boek, E. S., Hall, C. & Tardy, P. M. J. Deep bed filtration modelling of formation damage due to particulate invasion from drilling fluids. *Transp. Porous Med.* **91**, 479–508. https://doi.org/10.1007/s11242-011-9856-0 (2012).

Author contributions

Heng FAN: Investigation, Conceptualization, Writing – original draft, Writing – review & editing, Funding acquisition.Chenglong Wang: Investigation, Writing – original draft, Formal analysis.Huizhen Liu (Corresponding author: lhz2485916980@163.com): Investigation, Writing – original draft, Simulation experiments.Weiwei Xiong: Conceptualization, Writing – review & editing.Zhonglong Tian: Methodology, Validation.

Declarations

Competing interests

The authors declare no competing interests.

Additional information

Correspondence and requests for materials should be addressed to H.L.

Reprints and permissions information is available at www.nature.com/reprints.

Publisher's note Springer Nature remains neutral with regard to jurisdictional claims in published maps and institutional affiliations.